IEEE Photonics Journal
An IEEE Photonics Society Publication

Highly Sensitive Photoacoustic Imaging: A New Strategy for Ultrahigh Spatial Resolution Seismic Physical Model Imaging

Volume 12, Number 3, June 2020

Xin Liu
Wen Wang
Qiangzhou Rong
Baozhi Yu

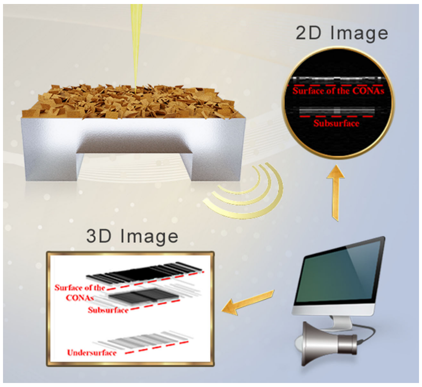

DOI: 10.1109/JPHOT.2020.2987342

Highly Sensitive Photoacoustic Imaging: A New Strategy for Ultrahigh Spatial Resolution Seismic Physical Model Imaging

Xin Liu,[1] **Wen Wang**,[1] **Qiangzhou Rong**,[1] **and Baozhi Yu**[2]

[1]School of Physics, Northwest University, Xi'an 710069, China
[2]Institute for Frontier Materials, Deakin University, Waurn Ponds, VIC 3216, Australia

DOI:10.1109/JPHOT.2020.2987342

Manuscript received March 2, 2020; revised April 1, 2020; accepted April 8, 2020. Date of current version April 28, 2020. This work was supported in part by the Natural Science Foundation under Grant 61605159, in part by the Natural Science Foundation of Shaanxi, China under Grants 2019JM-358, 2018JQ6011, and in part by the Shaanxi Education Department Fund under Grant 18JK0779. Corresponding authors: Qiangzhou Rong (e-mail: qzrong2010@gmail.com) and Baozhi Yu (e-mail: baozhi.yu@deakin.edu.au).

Abstract: Seismic-physical-model imaging (SPM), a successful strategy for the research in seismic wave propagation and wave theoretical predictions, effectively bridges the computation modeling and the field exploration and leads to a nearly ideal setting without a rock matrix. However, the current strategy for SPM imaging, the ultrasonic imaging technology, shows a narrow excitation frequency and a low coupling efficiency, which strongly limit the resolution of the image. Herein, laser ultrasonic imaging strategy, an imaging strategy which merges the large penetration depth of ultrasound imaging and high contrast of optical imaging, is developed for SPM imaging for the first time, where photoacoustic (PA) effect is utilized for the excitation. A customized contrast agent, $\mathrm{Co_3O_4}$ nanoflake arrays (CONAs), is designed for this special application of photoacoustic imaging in a large-scale via a facile hydrothermal method. The PA properties of the as-prepared CONAs are investigated with both theoretical and experimental methods. The results demonstrate the CONAs enhance the response signal over 16 times due to the strong light absorption, high photoacoustic-to-acoustic transformation efficiency and excellent thermal stability of the CONAs. By applying PA technology with the assistance of CONAs, 3D SPM images with high resolution are achieved.

Index Terms: Seismic-physical-model imaging, photoacoustic imaging, Laser ultrasonic technology, $\mathrm{Co_3O_4}$ nanoflake arrays.

Abbreviations

SPM	Seismic-physical-model
PA	Photoacoustic
CONAs	Co3O4 nanoflake arrays
PZT	Piezoelectric transducer
UW	Ultrasonic wave
LUT	Laser ultrasonic technology
SEM	Scanning electron microscopy

TEM	Transmission electron microscopy
HRTEM	High-resolution transmission electron microscopy
FFT	Fast Fourier Transform
XRD	X-ray diffraction
SNR	Signal to Noise Ratio

1. Introduction

Seismic physical model (SPM) imaging, an important strategy for the research in seismic wave propagation and wave theoretical predictions, includes the excitation of the signal, the collection the acoustic signal which carries the internal structure information of the model through ultrasonic transmission and scanning, and reconstruction of the three-dimensional model according to the inversion algorithm [1], [2]. The ultrasonic imaging technology is widely used for SPM imaging where a current-driven piezoelectric transducer (PZT) is used as the standard emission source [3], [4]. However, the narrow excitation frequency and low direct coupling efficiency strongly limit the quality of the images [5]. In addition, the wave shape of UW is determined by the PZT structure, resulting in a poor flexibility of the UW excitation. Therefore, a new strategy for SPM imaging is urgently desired. Photoacoustic (PA) imaging, which merges the large penetration depth of ultrasound imaging and high contrast of optical imaging, has been highlighted as one of the latest and most promising non-contact functional imaging method and widely applied in the field of biomedical preclinical and clinical, [6], [7] such as sentinel lymph node imaging, breast cancer imaging, brain imaging [8]–[13]. Based on the PA effect, the laser ultrasonic technology (LUT) can generate a strong ultrasonic wave field and form a broadband frequency acoustic source on the surface of large-scale objects. Compared to the traditional ultrasonic excitation with the PZT, LUT takes the outstanding properties of the broadband frequency, the high coupling efficiency and spatial resolution [14], [15]. However, LUT hasn‘t been developed for SPM imaging so far.

As is known, PA contrast agents is of great importance to the high-quality PA imaging. To date, a wide variety of contrast agents for PA imaging have been developed and reported, including noble metal nanoparticles, carbon nanotubes, graphene-based agents, 2D graphene analogues, organic nanoparticles, and semiconducting polymer nanoparticles (SPNs), and so on [16]–[26]. Nevertheless, nearly all the contrast agents are designed for bio-applications, where the agents are required to show low toxicity and immunogenicity, high target affinity and specificity, and high biocompatibility. An excellent photoacoustic contrast agent for SPM imaging should possess photophysical properties of low quantum yield, high molar-extinction coefficient, broadband light absorption, and excellent photostability as well as low cost, low environmental footprint [27], [28]. There are some common materials that can be potentials for SPM imaging, such as polymer nanoparticle-based materials, rubber and regular carbon fiber. However they present weak thermal stability with melting temperature and oxidation temperature. [29]–[31] In comparison, $\mathrm{Co_3O_4}$ is one of the promising PA contrast agents because of its low cost, environmentally friendly nature, excellent thermal and chemical stabilities (with 890°C thermal decomposition point), and a large nonlinear to linear absorption. [32]–[35] However, up to now, there is no report on developing $\mathrm{Co_3O_4}$ as a contrast agent for the PA imaging.

Based on the above considerations, LUT is developed for SPM imaging for the first time, where PA effect is utilized for the excitation. $\mathrm{Co_3O_4}$ nanoflake arrays (CONAs) are fabricated in a large-scale via a facile hydrothermal method and used as the contrast agent. The PA effects of CONAs film are simulated including light absorption, thermal expansion and acoustic pressure. The PA performance of CONAs film is tested at the same time and the response intensity of the CONAs film is over 16 times higher than that of Si substrate, which highly corresponds to the simulation results. Besides, the CONAs film works well even under a high power of 12 W. Furthermore, with the assistance of the CONAs, a 3D SPM morphology is imaged with high resolution, which contains its internal interface and external contour of SPM. To our best knowledge, the CONAs-based LUT hasn‘t been applied in SPM imaging up to now.

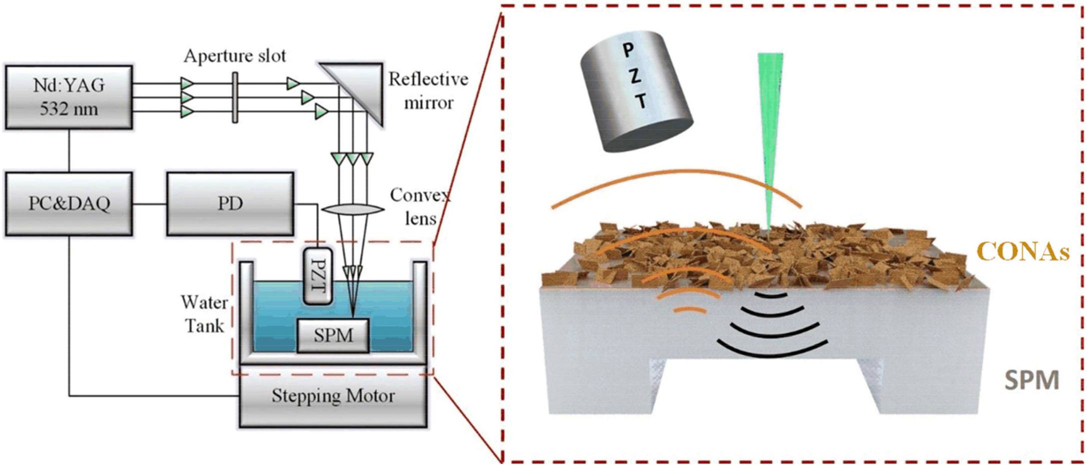

Fig. 1. (a) Experimental setup diagram (left) and schematic diagram of echo detection process (right).

2. Experimental Details

2.1 Synthesis of CONAs

In a typical experimental procedure, 0.623g $Co(CH_3COO)_2 \cdot H_2O$ and 1.4g $CO(NH_2)_2$ are added into a mixture of 5 mL ethanol and 15 mL deionized water. The obtained mixture is stirred for 30 min and then transferred into a Teflon-lined stainless-steel autoclave with a capacity of 50 ml. A 1.5 cm × 3 cm Si wafer is placed in the autoclave which is used as the substrate for the arrays. The autoclave was then sealed and hydrothermally treated at 160 °C for 2 h. The products were collected and washed by deionized water when the autoclave cools down to room temperature naturally. The obtained products are then annealed in air at 300 °C for 2 h and then collected.

2.2 Characterization of CONAs

Transmission electron microscope (TEM) and high-resolution transmission electron microscope (HRTEM) images were obtained on FEI Tecnai F20. S canning electron microscope (SEM) images were obtained on a FE-SEM Hitachi s-8600 microscope. X-ray diffraction (XRD) analysis was carried out using a D8 Advance, Bruker AXS Corporation, Germany. The ultraviolet-visible (UV-Vis) absorption spectra were recorded using a T6-1650F (Persee, Beijing) UV-Vis-NIR spectrophotometer.

2.3 Photoacoustic Performance Test and SPM Imaging

Referenced to the simulation, the SPM imaging was demonstrated experimentally. Fig. 1(a) demonstrates the schematic diagram of the experimental setup: a 532 nm Nd: YAG nanosecond laser (COHERENT Evolution-30) with a pulse duration of 200 ns, a repetition rate of 1 kHz, a maximum single pulse energy of 26 mJ and a beam diameter of $<$8.5 mm was used as the optical radiation source. The power and size of the laser spot were controlled by an optical attenuator and focusing lens. The laser beam is focused by a cylindrical lens into a line and focused on the prepared SPM surface. The PA was detected by a focusing PZT followed with an oscilloscope for picking signal. In order to improve the PA coupling efficiency, the prepared SPM model was placed in a water tank, and the PZT was immersed into the water and hanged over the upper surface of SPM. Only the longitudinal wave was detected by and analyzed. A simple plexiglas SPMs were prepared by 3D-printed technology, which simulated the simple geological structures (uplifting structure of natural scenario). The prepared CONAs films was attached onto the surfaces of SPM. Before attaching the film, the SPM surface was preprocessed to smooth and clean. Once the experiment setup was constructed, the laser excited the UW on the SPM surface, and the PZT detected the

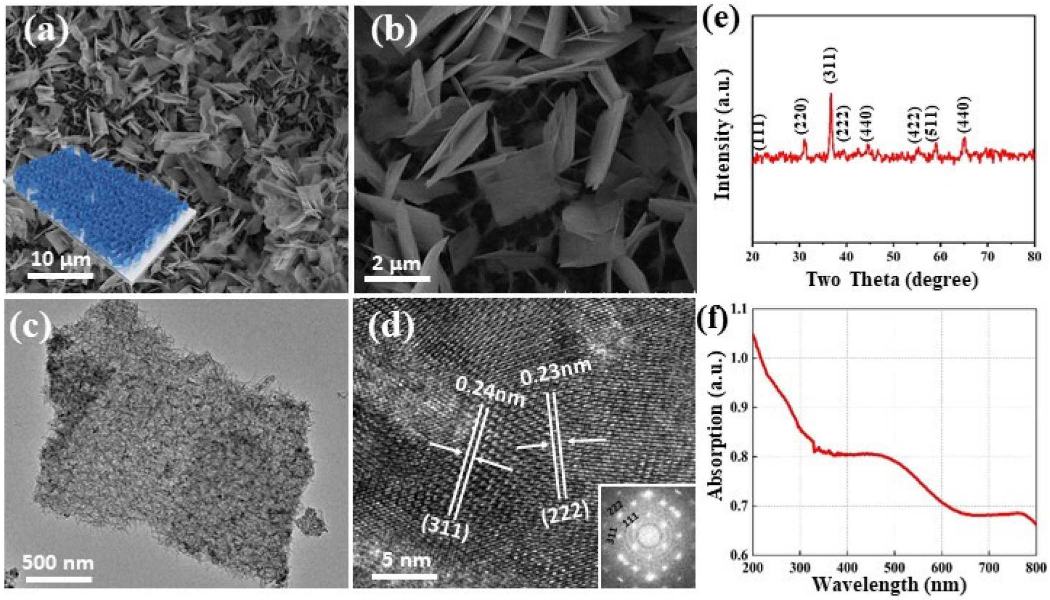

Fig. 2. (a) The low and (b) high magnification top-view SEM images of the obtained CONAs on the Si substrate; inset is the schematic diagram. (c) The TEM image, (d) the HRTEM image and its corresponding FFT pattern of CONAs, (e) the XRD pattern and (f) UV-Vis spectrum of Co_3O_4.

echo from the inside of SPM, as shown in Fig. 1(a) (right). After that, the images were constructed by the time-flight algorithm.

3. Results

3.1 Characterizations of CONAs

The CONA film is synthesized on a Si wafer via a hydrothermal method. The morphology of the obtained CONAs are investigated with scanning electron microscopy (SEM) and transmission electron microscopy (TEM). The top-view SEM image of CONAs on the Si substrate is presented in Fig. 2(a) and (b). Observed from the images, the ultrathin nanoflakes homogeneously distribute on the surface of the Si substrate. Detailed information of CONAs is further obtained from the TEM analysis. It can be clearly observed in the TEM image (Fig. 2(c)) that the product has an ultrathin flake-like morphology, which is consistent with SEM observation. High-resolution transmission electron microscopy (HRTEM) analysis in Fig. 2(d) shows lattice spacing about 0.24 nm and 0.23 nm, which corresponds to the (311) planes ($d = 2.47$ Å) and (222) planes of Co_3O_4, which is further confirmed by the corresponding Fast Fourier Transform (FFT) pattern. Fig. 2(e) shows the XRD patterns of the obtained products. The positions and relative intensities of diffraction peaks match well standard Co_3O_4 patterns (JCPDS card No. 42-1467). The UV-Vis spectrum of Co_3O_4 nanoflake was demonstrated in Fig. 2(f). The intense band appeared at 410 nm is attributed to the $O^{2-} \rightarrow Co^{2+}$ charge transfer with the electronic band gap energy of 2.07 eV, [33] and the slight absorption band at 690 nm is attributed to the $O^{2-} \rightarrow Co^{3+}$ charge transfer with the electronic band gap energy of 1.45 eV [34]. This spectrum confirms the strong visible light absorption of CONAs.

3.2 PA Effect of CONAs

3.2.1 Theoretical Simulation: It is necessary to further quantify the PA effect of Co_3O_4 film on the surface of SPM in details, assisting to build a rule for setting the experiment parameters. Therefore, a finite element model established by COMSOL Multiphysics was used to practically evaluate how the material properties and dimensions affect the PA generation efficiency with boundary constrain of water. The CONAs absorb the optical energy and convert it into heat, generating a temperature rise. The thermoelastic expansion from the temperature rise generates acoustic waves. The generated acoustic pressure can be expressed as $p_0(r) = \Gamma \mu_a(r) \Phi(r, \mu_a)$, [36] where Γ is called the Gruneisen coefficient, a dimensionless constant that represents the efficiency of the conversion of heat to pressure, μ_a is the optical absorption coefficient of the medium, and Φ is the light incident fluence. Therefore, the whole simulations were processed with "heat transfer by conduction" mode, "solid stress and strain" mode and "pressure acoustic" mode. For simplifying the operation, an axisymmetric model was built using cylindrical coordinate system, which explained PA waves generation and calculation, as shown in Fig. 3(a). In COMSOL model, the thickness of the Co_3O_4 layer, the thickness of Si substrate and the width of them were set as 5 μm, 800 μm and 200 μm, respectively. According to the theory of thermoelasticity, [37]–[39] the PA signals were calculated as a function of time due to the photothermal expansion of the Co_3O_4 layer and the water domain. PA wave propagates in the water domain in the form of bipolar wave, and the propagation after 600ns is shown in Fig. 3(b).

In the simulation, the following coupling variables were used: Gaussian laser pulse was used as the heat source by the energy transfer of the electromagnetic wave interaction with Co_3O_4 layer; the temperature rise in the Co_3O_4 layer and water medium was used as input in the linear elastic thermal expansion calculations of the Co_3O_4 layer and water domain in the structural mechanics analysis; the transient temperature distribution was used as the input for the structural mechanics analysis to calculate the strain/stress distribution inside the absorption domain; and the acoustic pressure agitated in the outer domain was solved by the pressure acoustic analysis. In this axisymmetric model, the setting of boundary conditions was critical to obtain accurate acoustic profiles. Additional boundary and domain conditions were used to truncate the size of model geometry domain. Perfectly matched layer was used to avoid reflection interference in electromagnetic wave loading. Spherical wave radiation boundary condition was used in the acoustics pressure generation to allow an outgoing spherical pressure wave to leave the modeling domain with the minimal reflections. In the caculations, the typical parameters of the Gaussian pulsed-laser referred to the commercial laser (Nd: YAG Coherent, Evolution) used in the experiment: wavelength $l =$ 532 nm, pulse energy $Q =$ 100 μJ$\sim$20 mJ, laser spot radius $r =$ 1 mm$\sim$10 mm, pulse duration τ_{w} $=$ 200 ns. At the same time, the parameters Co_3O_4 layer used in the models were set as: density: ρ = 6450 kg m^{-3}, Poisson coefficient: μ = 0.33, Young modulus: $E =$ 124 GPa, heat expansion coefficient: $\alpha = 3.466 \times 10^{-6}$ K^{-1}, heat capacity:$C_{\mathrm{p}} =$ 508 J kg^{-1} K^{-1}.

To avoid any phase change appearance at the interface of Co_3O_4-to-water, a single pulsed laser with low energy density of 1 mJ cm^{-2} was set, as the blue curve shown in Fig. 3(c). The red curve in Fig. 3(c) shows the temperature change of the Co_3O_4 surface. The temperature rise up to maximum after 70 ns, and then decrease down gradually. The temperature change process is attributated to thermal spread delay after pulse radiation. The curve was employed as the input for calculating strain field distribution over the surface of the Co_3O_4 layer by the solid stress and strain mode. The acoustic pressure was calculated with the strain field as the input parameters of pressure acoustic mode and the results are obtained, shown in Fig. 3(d). It can be found that the acoustic pressure generated with Co_3O_4 layer is over 11 times higher than the acoustic pressure generated with Si substrate. This demonstrate that the Co_3O_4 has the strong PA effect for acoustic wave generation. Next, study the effect of laser parameters on the photoacoustic signal of Co_3O_4. The illumination diameter is a key parameter which significantly influence the PA excitation. The illumination laser power was held at 1W, the radiation radius was adjusted from 75 μm to 150 μm. As shown in Fig. 3(e), the PA signal is clearly attenuated by increasing the radiation area. The laser energy density is another key factor to affect the PA emission. When keeping the laser time-delay at 200 ns, the generated PA signals were calculated at the laser power increasing from 1 W to 3 W. As seen in Fig. 3(f), the intensity of acoustic signal is proportional to the laser power as well as they present a linear relation as the inset shown in Fig. 3(f). The above theoretical simulation and simulation have guiding significance to the experiment.

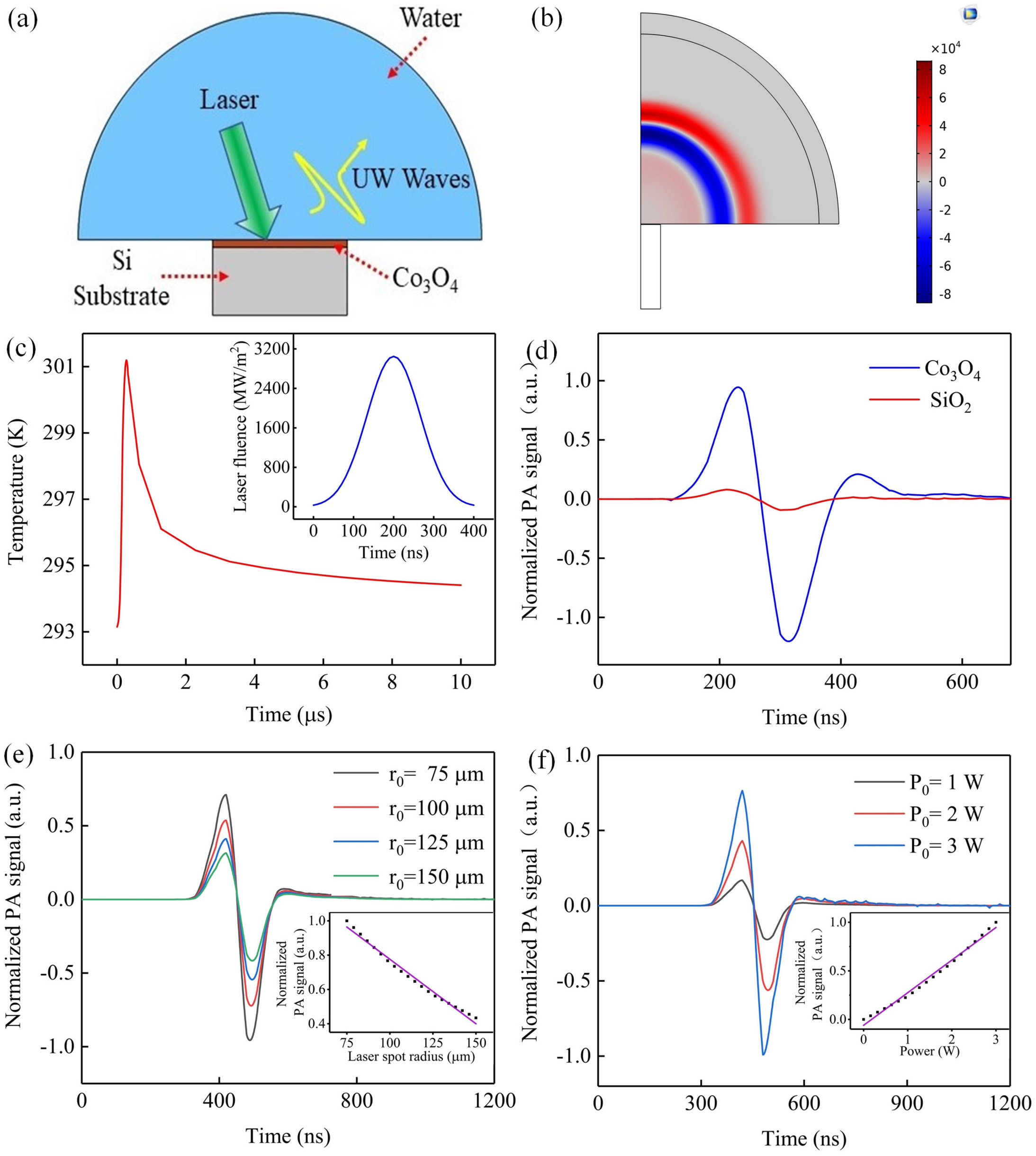

Fig. 3. (a) Scheme diagram of PA excitation, (b) Sound pressure distribution in the water domain under 600 ns pulsed laser illumination. (c) Temperature change curve and laser flux curve of material center point under laser illumination, (d) PA signals of different functional PA materials: Co_3O_4 and SiO_2. (e) PA signal generations with different laser beam diameters: the laser diameter is 75 μm, 100 μm, 125 μm and 150 μm, respectively. The interior illustration shows a linear relationship between spot radius and sound pressure (f) PA signal generations with different laser power: the laser power is 1 W, 2 W, 3 W, respectively. The internal illustration shows a linear relationship between laser power and sound pressure.

3.2.2 Experimental Results: The PA excitation test of the CONAs was also conducted. The test sample was prepared by attaching the CONAs film with SiO_2 as a substrate on an uplifting-type SPM. The SPM contains a step profile inside model. The material of SPM was set as plexiglass that has the low acoustic impedance and the several centimeter scales. A pulse laser was used as illumination source, and a PZT was used as the detector. The sample was placed into a water

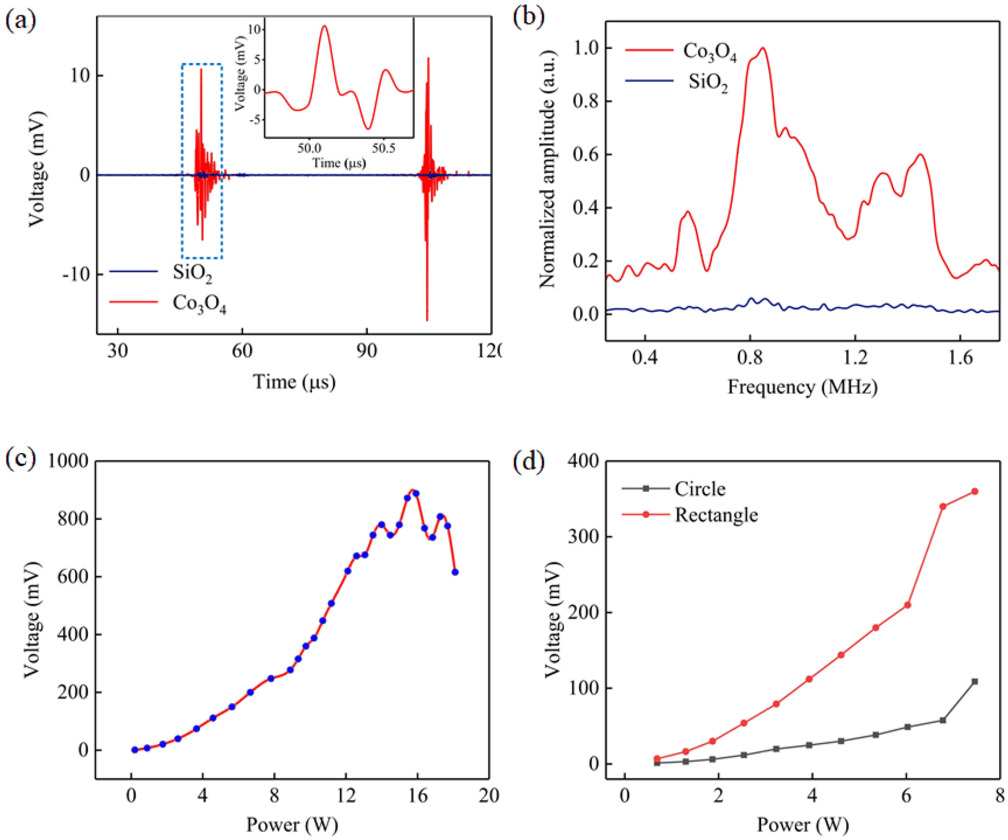

Fig. 4. Collected PA echo signals from SPM attached of CONAs and SiO$_2$ substrate, (a) time-domain signal, (b) frequency-domain transformed by (a), (c) relationship between laser power and PA intensity, (d) PA generation by both rectangular excitation and circular excitation.

tank to improve the coupling of acoustic-to-PZT. As shown in Fig. 4(a), when illuminating the sample surface, a strong UW signal was observed with a clear bipolar head wave that is coincident with the theoretical simulation. The appearance of the extra tail oscillation was caused by the aftershock of CONAs. The separate peaks are the echo signals from the different interfaces of the SPM inside. The time gap between two peaks can present the position information of interfaces. In comparison, as the laser illuminated the SiO$_2$ substrate also attached on the SPM, the echo signal was recorded as the blue curve shown in Fig. 4(a). Its intensity is much lower than that of CONAs since the weak PA efficiency of SiO$_2$. In order to analyze the frequency of the generated CONAs PA signal, both time-domain signals were transferred to the frequency spectra, as shown in Fig. 4(b). It characterizes the frequency components of CONAs PA signal, which presents a wide band. Compared with the narrow frequency band of the PZT source, this is more in line with the requirements for seismic sources in actual seismic wave detection. The main frequency is posited around the 1 MHz that is determined by the PZT resonance frequency. Compared with SiO$_2$, the PA signal generated by CONAs increase over 16 times, and SNR increase up to 30.51 dB. This result well testifies the strong PA generation coming from the CONAs.

According to theoretical simulation described above, the excited PA signal intensity should be proportional to the laser power. In experiment, as expected, when increasing the laser power from 0 W to 18 W, the UW signal increased up to a maximum value and fluctuated in a small range. The peak-to-peak voltage of UW signal was recorded and plotted as the function of the laser power, as shown in Fig. 4(c). It seen that, in the lower laser power region, the excited UW pressure is linearly relative to the laser power. When laser was up to 14 W (about the saturation absorption value of

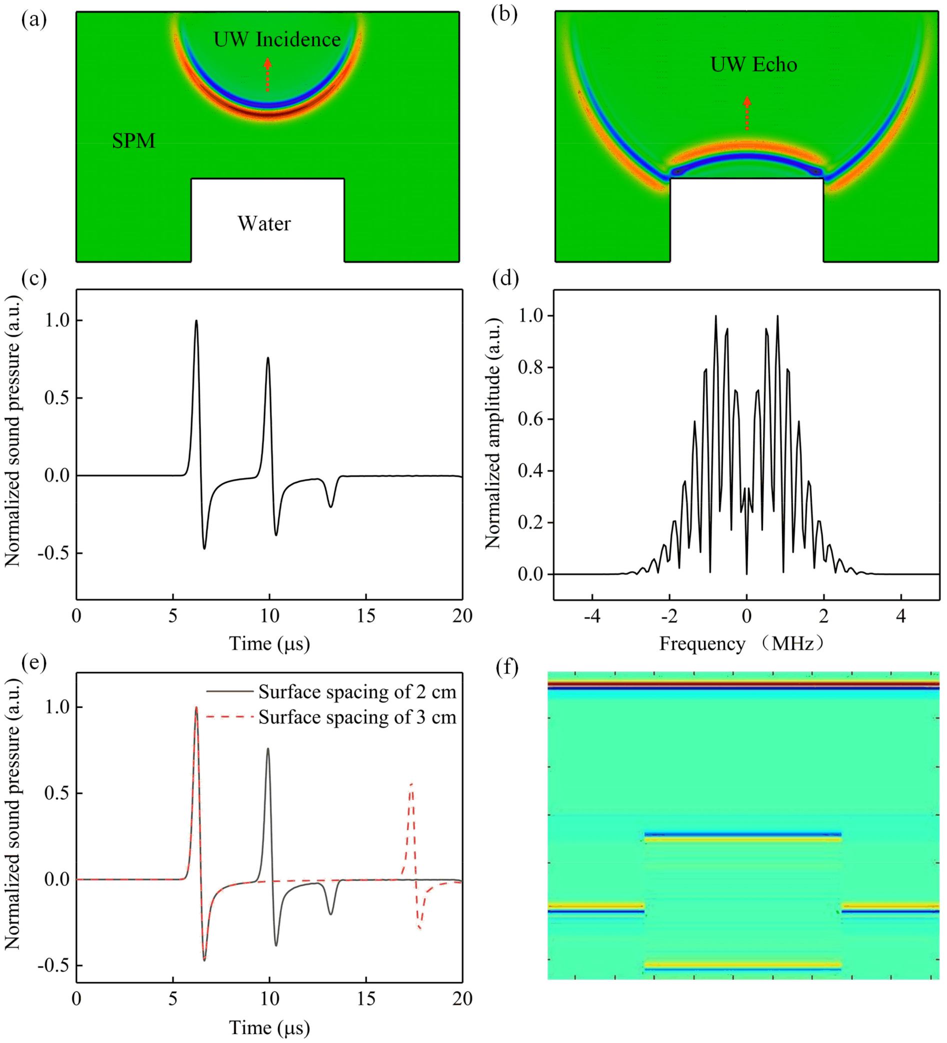

Fig. 5. Numerically simulated SPM imaging, (a) the PA transmits into SPM, (b) the partial UW was reflected by the inside arched profile, (c) the recorded time-domain signals and frequency-domain signals, (e) the time delay of echo from the reflections of different positions on the surface of inside structure, and (f) the reconstructed images of SPM by the time-flight algorithm.

CONAs), the PA signal tends to a stable value. With the laser power further increasing larger, the PA signal appeared the apparent fluctuation that was mainly caused by the thermal-induced air bubble generation on the CONAs film. Finally, the CONAs film is gradually burnt to be broken after the stronger laser illumination for several seconds. This result explained from the side that CONAs has good photothermal stability. Moreover, we compared the PA signals excited by the rectangular and circular light, as shown in Fig. 4(d). The rectangular light excitation presents the larger PA signal generation because its larger illumination area. In experiment, it therefore works as a large-scale source for fast 3D SPM scanning imaging so that it was finally chosen as the excitation method.

3.3 SPM Imaging With CONAs

3.3.1 Theoretical Simulation: The SPM imaging was here simulated by COMSOL Multiphysics for guiding experiment and image reconstruction, of which a PA source and a detector were set to launch the UW and pick up echo data. The detector was installed on the surface of SPM and

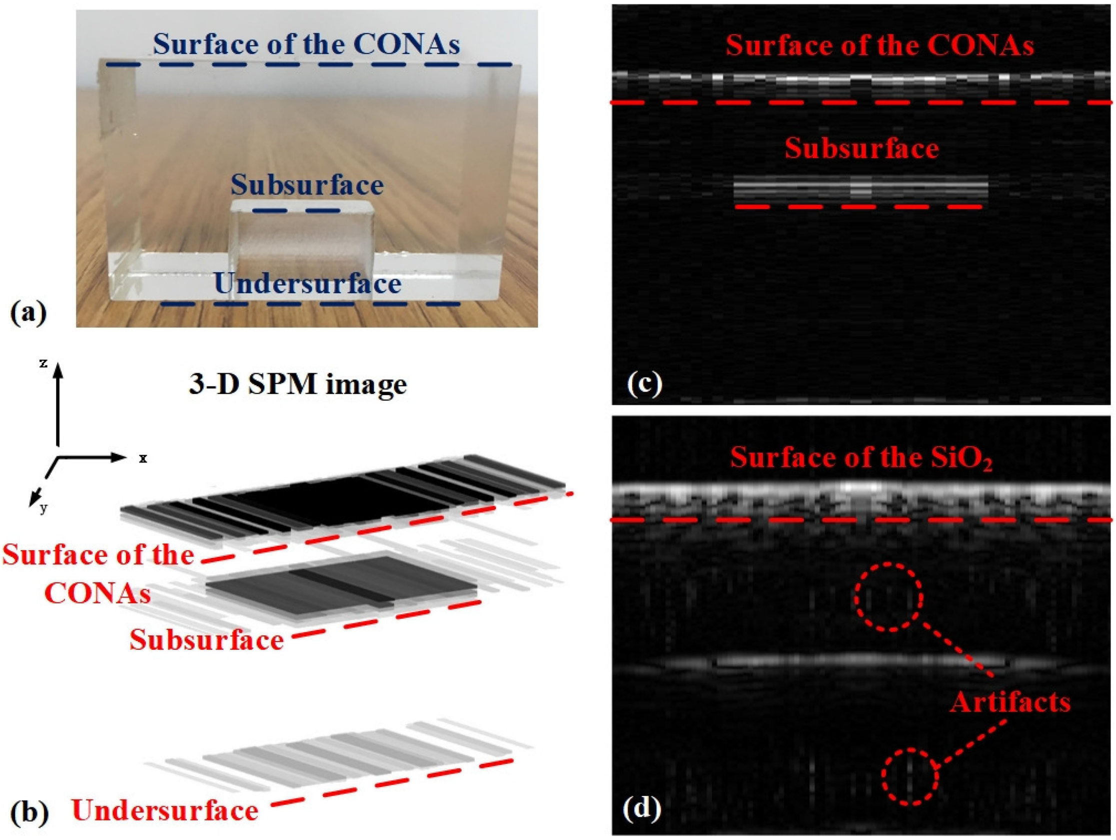

Fig. 6. (a) Optical image of the SPM, (c) the 3D SPM reconstruction imaging with CONAs, (c) the 2D SPM reconstruction imaging with CONAs, (d) the 2-D SPM reconstruction imaging with SiO_2.

was set to hang over the excitation point. The contours of UW travel and reflection were displayed in Fig. 5(a) and (b). The forwards wave propagated into the SPM, and then the partial wave was reflected at the step interface. Fig. 5(c) showed collected echo signals received by the detector from different interfaces, the time delay between two signal peaks was corresponding to the distance of the reflection surfaces. Therefore, the original model can be recovered by inversion of time delay between the signal peaks. In order to correspond to PZT used in the experiment, the main frequency is set at 1 MHz. The frequency-domain signal was obtained by FFT from time-domain signals, as shown in Fig. 5(d). And then the source and detector were controlled to move along the surface by a step of 2 mm, simulating the process of scanning detection. The two interfaces with a depth difference of 1 cm generated a time delay of approximately 8 μs, as shown in Fig. 5(e). In isotropic media, the echo signals from different interfaces have the time delay at the peak, which are only determined by the distance between the interfaces Δs and the sound velocity of the medium v_s, the time delay $t_d = 2\Delta s/v_s$. After reconstructing the all seismic data by the inverse time algorithm, both the upper surface and the step interface inside SPM profiles were observed clearly as expected, as shown in Fig. 5(f) [40].

3.3.2 Experimental Results: The SPM imaging performance of CONAs was investigated on a SPM, SPM simulated the simple geological structures (uplifting structure of natural scenario). The photograph of the SPM is shown in Fig. 6(a). After the collecting and reconstructing the seismic signals, as shown in Fig. 6(b), a three-dimensional image was observed that displayed three interfaces clearly. And the SPM imaging was performed without CONAs coating on the SPM surface. In comparison, two-dimensional images of both with- and without CONAs are reconstructed in Fig. 6(c) and d. It is seen that, with the assistance of CONAs, the image in Fig. 5(d) presents higher resolution and fewer artifacts than that in Fig. 6(d). Here, for the imaging, the lateral resolution is 500 μm that is determined by the step size of scanning motor, and the axial resolution is 600 μm that is determined by the frequency (1 MHz) of transducer [6].

These artifacts may be generated by the electrical or environmental noise of the imaging system, and improving the SNR of the signal can effectively reduce the artifacts. [37] The improvement of the imaging quality is mainly contributed to the intensity increase of the PA signal on the SPM surface, which assists to obtain a high SNR at the frequency of 1 MHz. Based on the strong PA excitation of CONAs, the laser-ultrasonic technology can be used for the large-scale SPM imaging.

3.4 Discussion

According to the results mentioned above, the SPM imaging quality using the laser-ultrasonic technology is highly relevant to the PA excitation efficiency that is determined by the surface material of SPM. The CONAs presented several advantages: a) Strong absorption to light: because of the $O^{2-} \rightarrow Co^{2+}$ and $O^{2-} \rightarrow Co^{3+}$ bandgap energy transitions, Co_3O_4 has a bandgap size at 1.45 eV and 2.07 eV, which corresponds to 690 nm and 410 nm, respectively. Therefore, CONAs has a great performance in terms of optical absorption and thermal-to-acoustic transformation at 532 nm; b) The excellent thermal and chemical stability: Co_3O_4 decomposes into forming cobaltic oxide (CoO) and interacts with atmospheric oxygen giving Co_2O_3 at the temperature higher than 800 °C. It presents the CONAs has the thermal and chemical stability at the high laser power illumination up to 27 W cm^{-2}; c) Suitable for batch application: CONAs-based thin film is easy to be synthesized by hydrothermal, and also is mass-produced with low cost. Based on these outstanding performances, CONAs can be a good transducer to promote the PA excitation, and widely applied to SPM imaging.

4. Conclusions

In summary, LUT is developed for SPM imaging, where photoacoustic (PA) effect is utilized for the excitation. A customized contrast agent, Co_3O_4 nanoflake arrays, is designed for this special application of photoacoustic imaging in a large-scale via a facile hydrothermal method. The PA properties of the as-prepared Co_3O_4 nanoflake arrays are investigated with both theoretical and experimental methods. The results demonstrate the Co_3O_4 nanoflake arrays enhance the response signal over 16 times due to the strong light absorption, high photoacoustic-to-acoustic transformation efficiency and excellent thermal stability of the Co_3O_4 nanoflake arrays. By applying PA technology with the assistance of Co_3O_4 nanoflake arrays, 3D SPM images with high resolution are achieved. To the best of our knowledge, our study not only reported a low cost, batch preparation and excellent film-forming PA contrast agent in the near-infrared region, which suitable for large SPM imaging, but also first applied the PA method to SPM imaging which greatly improved the imaging quality. We believe that this study provides a new method for further improving the resolution of SPM imaging and can better combine theoretical models with practical exploration.

References

[1] L. K. Santos, “Seismic physical modeling based on the physical similitudes: application in isotropic media,” Master’s Diss., Federal Univ. Pará, 2015.
[2] D. Draganov, X. Campman, J. Thorbecke, A. Verdel, and K. Wapenaar, “Seismic exploration-scale velocities and structure from ambient seismic noise (>1 Hz),” *J. Geophysical Res.: Solid Earth*, vol. 118, no. 8, pp. 4345–4360, 2013.
[3] T. R. Gururaja, W. A. Schulze, L. E. Cross, R. E. Newnham, B. A. Auld, and Y. J. Wang, “Piezoelectric composite materials for ultrasonic transducer applications. part I: Resonant modes of vibration of PZT rod-polymer composites,” *IEEE Trans. Sonics Ultrasonics*, vol. 32, no. 4, pp. 481–498, 1985.
[4] J. Jung *et al.*, “31-mode piezoelectric micromachined ultrasonic transducer with PZT thick film by granule spraying in vacuum process,” *Appl. Phys. Lett.*, vol. 110, no. 21, 2017.
[5] Y. Ling, “The study of the laser-induced ultrasonic waves propagating in materials with continuous elstic properties changes of near-surface layer,” Ph. D. Diss., Naning Univ. Sci. Technol., 2008.

[6] L. V. Wang and S. Hu, "Photoacoustic tomography: in vivo imaging from organelles to organs," *Science*, vol. 335, no. 6075, pp. 1458–62, Mar. 23, 2012.

[7] J. Weber, P. C. Beard, and S. E. Bohndiek, "Contrast agents for molecular photoacoustic imaging," *Nat Methods*, vol. 13, no. 8, pp. 639–50, Jul. 28, 2016.

[8] P. K. Upputuri, K. Sivasubramanian, C. S. Mark, and M. Pramanik, "Recent developments in vascular imaging techniques in tissue engineering and regenerative medicine," *Biomed. Res. Int.*, vol. 2015, 2015, Art. no. 783983.

[9] R. Li *et al.*, "Assessing breast tumor margin by multispectral photoacoustic tomography," *Biomed. Opt. Express*, vol. 6, no. 4, pp. 1273–81, Apr. 1, 2015.

[10] M. Anastasio *et al.*, "Recent advancement in transcranial brain imaging using photoacoustic computed tomography," *J. Acoustical Soc. America*, vol. 135, no. 4, pp. 2208–2208, 2014.

[11] T. N. Erpelding *et al.*, "Sentinel lymph nodes in the rat: noninvasive photoacoustic and US imaging with a clinical US system," *Radiology*, vol. 256, no. 1, pp. 102–10, Jul. 2010.

[12] M. Pramanik and L. V. Wang, "Thermoacoustic and photoacoustic sensing of temperature," *J. Biomed. Opt.*, vol. 14, no. 5, Sep./Oct. 2009, Art. no. 054024.

[13] X. Cai, C. Kim, M. Pramanik, and L. V. Wang, "Photoacoustic tomography of foreign bodies in soft biological tissue," *J. Biomed. Opt.*, vol. 16, no. 4, Apr 2011, Art. no. 046017.

[14] P. N. J. R. Bruno Pouet, Ultrasonic intrinsic attenuation measurement using laser techniques (Ultrasonics Symposium). 1989.

[15] I. Arias, "Modeling of the detection of surface-breaking cracks by laser ultrasonics," Doctor Philosophy Diss., Northwestern Univ., 2003.

[16] H. Zhu *et al.*, "Cobalt nanowire-based multifunctional platform for targeted chemo-photothermal synergistic cancer therapy," *Colloids Surf B Biointerfaces*, vol. 180, pp. 401–410, Aug. 1, 2019.

[17] W. Li, P. K. Brown, L. V. Wang, and Y. Xia, "Gold nanocages as contrast agents for photoacoustic imaging," *Contrast Media Mol. Imag.*, vol. 6, no. 5, pp. 370–7, Sep./Oct. 2011.

[18] J. Chen *et al.*, "Gold nanocages: A novel class of multifunctional nanomaterials for theranostic applications," *Adv. Functional Mater.*, vol. 20, no. 21, pp. 3684–3694, 2010.

[19] S. E. Skrabalak, L. Au, X. Li, and Y. Xia, "Facile synthesis of Ag nanocubes and Au nanocages," *Nat. Protoc*, vol. 2, no. 9, pp. 2182–90, 2007.

[20] T. Kim, Q. Zhang, J. Li, L. Zhang, and J. V. Jokerst, "A gold/silver hybrid nanoparticle for treatment and photoacoustic imaging of bacterial infection," *ACS Nano*, vol. 12, no. 6, pp. 5615–5625, Jun. 26, 2018.

[21] J. Wang *et al.*, "Eumelanin-Fe3O4 hybrid nanoparticles for enhanced MR/PA imaging-assisted local photothermolysis," *Biomater Sci*, vol. 6, no. 3, pp. 586–595, Feb. 27, 2018.

[22] T.-T. D. Pham *et al.*, "Ordered assemblies of Fe3O4 and a donor-acceptor-type π-conjugated polymer in nanoparticles for enhanced photoacoustic and magnetic effects," *Polymer*, vol. 161, pp. 205–213, 2019.

[23] X. Chen *et al.*, "Rational design of branched Au-Fe3 O4 janus nanoparticles for simultaneous trimodal imaging and photothermal therapy of cancer cells," *Chemistry*, vol. 23, no. 68, pp. 17204–17208, Dec. 6, 2017.

[24] Q. Han *et al.*, "Rational design of Fe3O4@C nanoparticles for simultaneous bimodal imaging and chemo-photothermal therapy in vitro and in vivo," *J. Mater. Chemistry B*, vol. 6, no. 34, pp. 5443–5450, 2018.

[25] W. Wang, C. Hao, M. Sun, L. Xu, C. Xu, and H. Kuang, "Spiky Fe_3O_4@Au supraparticles for multimodal in vivo imaging," *Adv. Functional Mater.*, vol. 28, no. 22, 2018.

[26] H. Fu *et al.*, "Zinc oxide nanoparticle incorporated graphene oxide as sensing coating for interferometric optical microfiber for ammonia gas detection," *Sensors and Actuators B: Chem.*, vol. 254, pp. 239–247, 2018.

[27] R. G. Pratt, "Seismic waveform inversion in the frequency domain, Part 1: Theory and verification in a physical scale model," *Geophysics*, vol. 64, no. 3, pp. 888–901, 1999.

[28] Q. Rong *et al.*, "UW Imaging of Seismic-Physical-Models in Air Using Fiber-Optic Fabry-Perot Interferometer," *Sensors*, vol. 17, no. 2, p. 397, 2017.

[29] Z. Jie, S. Feng, and Q. Ma, "Kinetics of the thermal degradation and thermal stability of conductive silicone rubber filled with conductive carbon black," *J. Appl. Polym. Sci.*, vol. 89, no. 6, pp. 1548–1554, 2003.

[30] X. Wang and W. Dou, "Preparation of graphite oxide (GO) and the thermal stability of silicone rubber/GO nanocomposites," *Thermochimica Acta*, vol. 529, no. none, pp. 25–28.

[31] H. H. Gibbs, R. C. Wendt, and F. C. Wilson, "Carbon fiber structure and stability studies," *Polym. Eng. Sci.*, vol. 19, 1979.

[32] A. H. H. Al-Masoodi *et al.*, "Cobalt oxide nanocubes thin film as saturable absorber for generating Q-switched fiber lasers at 1 and 1.5 μm in ring cavity configuration," *Opt. Fiber Technol.*, vol. 45, pp. 128–136, 2018.

[33] P. Jagriti and C. Pratima, "Study of physical properties of cobalt oxide (Co3O4) nanocrystals," *Mater. Characterization*, vol. 61, no. 5, pp. 575–579, 2010.

[34] H. Zhu*et al.* "Cobalt nanowire-based multifunctional platform for targeted chemophotothermal synergistic cancer therapy," *Colloids Surfaces B:Biointerfaces*, vol. 180, pp. 401–410, 2019.

[35] D. Barreca *et al.*, "Composition and Microstructure of cobalt oxide thin films obtained from a novel cobalt(II) precursor by chemical vapor deposition," *Chemistry Mater.*, vol. 13, no. 2, pp. 588–593.

[36] K. L. Bell, "Photoacoustic remote sensing (PARS) microscopy," *Doctor of Philosophy Biomed. Eng.*, 2019.

[37] L. V. Wang, *Photoacoustic Imaging And Spectroscopy*, CRC Press, 2009.

[38] E. P. Furlani, I. H. Karampelas, and Q. Xie, "Analysis of pulsed laser plasmon-assisted photothermal heating and bubble generation at the nanoscale," *Lab A Chip*, vol. 12, no. 19, p. 3707.

[39] A. O. Govorov *et al.*, "Gold nanoparticle ensembles as heaters and actuators: Melting and collective plasmon resonances." *Nanoscale Res. Lett.*, vol. 1, no. 1, pp. 84–90, 2006.

[40] H. Peng, *Introduction to Ultrasonic Imaging Algorithms*, China Univ. Sci. Technol. Press, 2008.